

**Structural and magnetic properties of FePt-Tb alloy thin films**N. Y. Schmidt<sup>1</sup>, S. Laureti,<sup>2</sup> F. Radu,<sup>3</sup> H. Ryll,<sup>3</sup> C. Luo,<sup>3,6</sup> F. d'Acapito,<sup>4</sup> S. Tripathi,<sup>5</sup> E. Goering,<sup>5</sup> D. Weller,<sup>1</sup> and M. Albrecht<sup>1</sup><sup>1</sup>*Institute of Physics, University of Augsburg, Universitätsstrasse 1, D-86159, Augsburg, Germany*<sup>2</sup>*Istituto di Struttura della Materia – CNR, 00016 Monterotondo Scalo, Rome, Italy*<sup>3</sup>*Helmholtz-Zentrum Berlin, D-14109 Berlin, Germany*<sup>4</sup>*CNR-IOM-OGG c/o ESRF, GILDA CRG, C/o ESRF BP220, F-38043 Grenoble, France*<sup>5</sup>*Max Planck Institute for Intelligent Systems, Heisenbergstrasse 3, D-70569 Stuttgart, Germany*<sup>6</sup>*Experimental Physics of Functional Spin Systems, Technische Universität München, James-Franck-Str. 1, 85748 Garching b. München, Germany*

(Received 18 December 2018; revised manuscript received 1 August 2019; published 28 August 2019)

We have studied structural and magnetic properties of  $(\text{FePt})_{1-x}\text{Tb}_x$  thin films grown at elevated temperatures on MgO(100) substrates. The incorporation of Tb into the chemically ordered  $L1_0$  FePt lattice gives rise to considerable changes in the structural and magnetic properties, depending on the Tb content and the deposition temperature. When grown at 770 °C, pronounced  $L1_0$  ordering of the initial FePt phase is present. It vanishes gradually with Tb addition, thereby forming additional crystalline Tb-Pt phases at higher Tb content. These structural changes are accompanied by a strong reduction of the perpendicular magnetic anisotropy with increasing Tb content, finally resulting in a soft magnetic material with in-plane easy-axis magnetization. Extended x-ray absorption fine-structure measurements were performed to examine the possible incorporation of Tb into the FePt lattice. Based on the number of Pt first neighbors, the transformation from the initial tetragonal  $L1_0$  structure to the chemically disordered fcc ( $A1$ ) phase with increasing Tb content could be firmly concluded. In a further sample series, FePt was grown at a lower temperature of 530 °C, which leads to reduced initial  $L1_0$  chemical ordering. Adding Tb results in strong elastic stress in the lattice, eventually causing full amorphization of the film. Interestingly, in this case, a spin-reorientation transition from in-plane to out-of-plane magnetic easy axis is found at low temperatures, which is associated with an anisotropic chemical short-range order present in the amorphous phase. Furthermore, x-ray magnetic circular dichroism studies at the Fe  $L_{3,2}$  and Tb  $M_{5,4}$  edges for all samples reveal strong antiferromagnetic coupling between Fe and Tb, resulting in a reduction of the net magnetization of the film.

DOI: [10.1103/PhysRevB.100.064428](https://doi.org/10.1103/PhysRevB.100.064428)**I. INTRODUCTION**

Chemically ordered  $L1_0$  FePt alloy thin films exhibiting large perpendicular magnetic anisotropy (PMA) of up to 7 MJ/m<sup>3</sup> [1–3] are being implemented in data storage media for heat-assisted magnetic recording, which is expected to extend the current areal density of 1 Tb/in.<sup>2</sup> toward 3–4 Tb/in.<sup>2</sup> [4–8]. The material properties of FePt can be tailored by adding third elements, e.g. Mn, Cu, Ni, Au, Ag, or Ir, allowing control of the magnetic anisotropy, the Curie temperature, and the crystallographic orientation as well as lowering the ordering temperature during postannealing of chemically disordered FePt films [9–19]. Also, the inclusion of rare-earth elements can provide further functionalities [20]. For example, the addition of Nd, a light rare-earth element, has previously been studied, resulting in a large enhancement of the saturation magnetization of  $L1_0$  chemically ordered FePt thin films due to ferromagnetic coupling of the magnetic moments between Fe and Nd, making it a potential material for permanent magnets and sensor applications [21]. By contrast, adding heavy rare-earth elements, e.g., Tb, should result in a strong reduction of the net magnetization due to the expectation of strong antiferromagnetic coupling

between Fe and Tb magnetic moments [22]. Furthermore, it has been shown that the magnetization dynamics of soft ferromagnetic thin films can be tuned using rare-earth dopants. For instance, for permalloy thin films, the Gilbert damping parameter can be varied over two orders of magnitude by addition of Tb [23]. These aspects are in particular interesting for laser-induced magnetic reversal processes using circularly polarized laser light, where the magnetic orientation can be set by the helicity of the laser pulses [24,25], as demonstrated for ferrimagnetic Tb-Fe alloys [26–29], therefore providing an intriguing pathway for overcoming the material constraints of high magnetic anisotropy. In this regard, it has been shown that a low remanent magnetization is required to obtain helicity-dependent all-optical switching [30,31], whereas high magnetization values typically result in dominant dipolar-driven reversal processes.

In this study, we have investigated the impact of Tb as a third element to  $L1_0$  ordered FePt thin films on their structural and magnetic properties. It is expected that Tb will couple antiferromagnetically to Fe, forming a ferrimagnetic material system with high magnetic anisotropy and reduced net magnetization, which might be relevant for effective all-optical switchability [30,31].

TABLE I. Overview of the two  $(\text{FePt})_{100-x}\text{Tb}_x$  sample series.

Sample name	Composition (at. %)	Thickness (nm)	Capping (3 nm)	$T_{\text{sub}}$ ( $^{\circ}\text{C}$ )
Series I				
FePt	$\text{Fe}_{51}\text{Pt}_{49}$	9.0	Al	530
$(\text{FePt})_{95}\text{Tb}_5$	$(\text{Fe}_{51}\text{Pt}_{49})_{95}\text{Tb}_5$	10	Al	530
$(\text{FePt})_{89}\text{Tb}_{11}$	$(\text{Fe}_{47}\text{Pt}_{53})_{89}\text{Tb}_{11}$	10.9	Al	530
$(\text{FePt})_{86}\text{Tb}_{14}$	$(\text{Fe}_{48}\text{Pt}_{52})_{86}\text{Tb}_{14}$	11.2	Al	530
$(\text{FePt})_{85}\text{Tb}_{15}$	$(\text{Fe}_{48}\text{Pt}_{52})_{85}\text{Tb}_{15}$	11.6	Al	530
$(\text{FePt})_{82}\text{Tb}_{18}$	$(\text{Fe}_{51}\text{Pt}_{49})_{82}\text{Tb}_{18}$	12.1	Pt	530
$(\text{FePt})_{80}\text{Tb}_{20}$	$(\text{Fe}_{48}\text{Pt}_{52})_{80}\text{Tb}_{20}$	11.8	Al	530
$(\text{FePt})_{72}\text{Tb}_{28}$	$(\text{Fe}_{50}\text{Pt}_{50})_{72}\text{Tb}_{28}$	10.5	Al	530
Series II				
FePt	$\text{Fe}_{50}\text{Pt}_{50}$	9.0	$\text{Si}_3\text{N}_4$	700
$(\text{FePt})_{95}\text{Tb}_5$	$(\text{Fe}_{50}\text{Pt}_{50})_{95}\text{Tb}_5$	9.3	$\text{Si}_3\text{N}_4$	700
$(\text{FePt})_{94}\text{Tb}_6$	$(\text{Fe}_{48}\text{Pt}_{52})_{94}\text{Tb}_6$	9.5	Al	770
$(\text{FePt})_{90.5}\text{Tb}_{9.5}$	$(\text{Fe}_{51}\text{Pt}_{49})_{90.5}\text{Tb}_{9.5}$	11.0	Al	770
$(\text{FePt})_{89}\text{Tb}_{11}$	$(\text{Fe}_{48}\text{Pt}_{52})_{89}\text{Tb}_{11}$	12.1	Al	770
$(\text{FePt})_{87}\text{Tb}_{13}$	$(\text{Fe}_{53}\text{Pt}_{47})_{87}\text{Tb}_{13}$	12.1	Al	770
$(\text{FePt})_{86}\text{Tb}_{14}$	$(\text{Fe}_{51}\text{Pt}_{49})_{86}\text{Tb}_{14}$	12.7	Al	770
$(\text{FePt})_{81.5}\text{Tb}_{18.5}$	$(\text{Fe}_{50}\text{Pt}_{50})_{81.5}\text{Tb}_{18.5}$	13.9	Al	770

## II. EXPERIMENTAL

Two series of  $(\text{FePt})_{1-x}\text{Tb}_x$  thin films were sputter deposited on  $\text{MgO}(100)$  substrates at  $530^{\circ}\text{C}$  (series I) and  $700\text{--}770^{\circ}\text{C}$  (series II). Codeposition of Fe, Pt, and Tb using individual targets was used at an Ar pressure of  $p_{\text{Ar}} = 3.5 \mu\text{bar}$ . The Tb content  $x$  was varied in the range 5–28 at. % by altering the Tb deposition rate while keeping the Fe and Pt rates constant. Thickness and composition were analyzed by Rutherford backscattering spectrometry (RBS). The total film thickness rises from 9 to 14 nm with increasing Tb content as Tb is just added to equiatomic FePt. Furthermore, for all these samples, 3-nm-thick capping layers (Al, Pt, or  $\text{Si}_3\text{N}_4$ ) were deposited at room temperature to avoid surface oxidation. An overview of the relevant sample parameters is given in Table I.

The magnetic characterization was performed using a superconducting quantum interference device-vibrating sample magnetometer (SQUID-VSM) in the temperature range 25–330 K. For selected samples, cross-section transmission electron microscopy (TEM) studies were performed, while the surface morphology was analyzed by atomic force microscopy (AFM). In addition, x-ray magnetic circular dichroism (XMCD) absorption experiments were performed at the high-field end station VEKMAG [32] installed at the PM2 beamline of the Helmholtz-Zentrum Berlin (HZB). X-ray absorption spectra were acquired at the Fe  $L_{2,3}$  and Tb  $M_{4,5}$  edges ( $3d^{10}4f^n \rightarrow 3d^94f^{n+1}$  transition) using total electron yield (TEY) detection. The XMCD signal was received by calculating the difference between x-ray absorption spectra measured with two opposite directions of the external magnetic field applied up to  $\pm 40$  kOe. Element-specific hysteresis loops were measured at 293 and 55 K at the  $L_3$  edge of Fe and the  $M_5$  edge of Tb at an energy where the XMCD signal had its maximum.

The structural properties regarding the  $L1_0$  structure and phase formation were investigated by x-ray diffraction (XRD)

using  $\text{Cu-K}\alpha$  radiation. In order to determine the local atomic environment of the Tb atoms in the FePt film volume, x-ray absorption spectroscopy (XAS) was used. XAS data were collected at the LISA-CRG beamline at the European Synchrotron Radiation Facility (Grenoble, France). The monochromator was equipped with a pair of Si(311) crystals used in dynamical focusing mode. A pair of Pd-coated mirrors was used for harmonic rejection and vertical beam focusing. Data collection was carried out at the Pt  $L_3$  (11 564 eV) edge. During data collection, the samples were kept at a temperature of 80 K to reduce thermal atomic vibrations, thereby enhancing the extended x-ray absorption fine structure (EXAFS) signal. The absorption coefficient was measured via fluorescence yield by using an energy-resolving (12)-elements high-purity germanium detector (energy resolution of about 250 eV). XAS data extraction and fitting were carried out with the ATHENA and ARTEMIS codes [33], while quantitative modeling was based on simulated EXAFS signals using the FEFF8.1 code [34].

## III. STRUCTURAL ANALYSIS

XRD ( $\theta$ – $2\theta$ ) scans of sample series I prepared at  $530^{\circ}\text{C}$  are shown in Figs. 1(a)–1(e). For pure FePt only a low intensity  $L1_0$ -(001) peak is detected, revealing the presence of a small amount of the chemically ordered  $L1_0$ -phase [Fig. 1(a)]. In addition, higher intensities of the  $L1_0$ -(002) FePt and of the A1-(002) peak of disordered FePt are observed, which overlap with the main  $\text{MgO}$ -(200) substrate peak intensity and cannot be well separated. With the addition of Tb up to 11 at. %, the weak  $L1_0$ -(001) peak shifts towards lower angles [Figs. 1(b) and 1(c)], while the overall intensities of

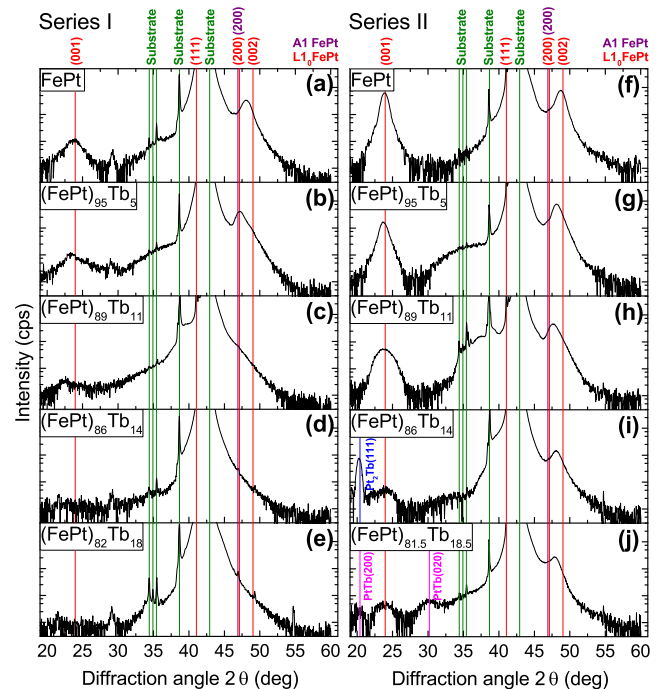


FIG. 1. XRD ( $\theta$ – $2\theta$ ) scans of  $(\text{FePt})_{100-x}\text{Tb}_x$  deposited (a)–(e) at  $530^{\circ}\text{C}$  (series I) and (f)–(j) at  $770^{\circ}\text{C}$  (series II). The additional peak at  $2\theta = 29.2^{\circ}$  is substrate related.

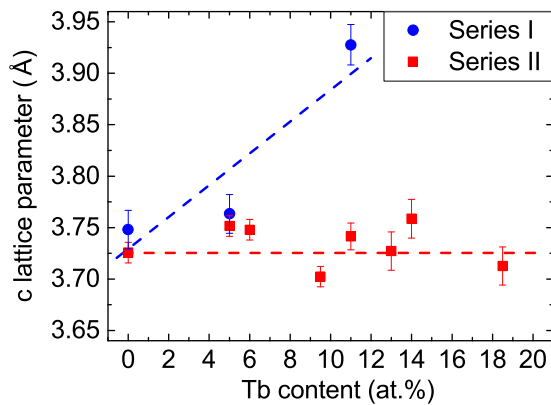


FIG. 2.  $c$ -lattice parameter extracted from the peak position of the  $L1_0$ -(001) superstructure reflection for both sample series. Dotted lines are guide to the eyes.

the  $L1_0$ -(002) and A1-(002) reflections are getting more and more reduced [Fig. 1(c)]. The  $c$ -lattice parameter was extracted from the peak position of the  $L1_0$ -(001) superstructure reflection, which increases drastically from 3.75 to 3.93 Å by adding up to 11 at. % of Tb (Fig. 2). Both shift and loss in (001) peak intensity hint at incorporation of Tb into the  $L1_0$  lattice presumably as an interstitial atom, which adds elastic stress to the lattice, eventually leading to full amorphization of the local Tb environment [Figs. 1(d) and 1(e)].

In order to promote the ordering process, FePt thin films were prepared at higher deposition temperatures up to 770 °C (series II, see Table I). The FePt reference sample revealed improved chemical  $L1_0$  ordering, as can be seen from the much higher intensities of the  $L1_0$ -(001) and (002) reflections [Fig. 1(f)]. However, it is difficult to extract the chemical order parameter due to the strong overlap of the peak intensities from FePt and the MgO(001) substrate. With increasing Tb content up to 11 at. %, the intensity of the  $L1_0$ -(001) superstructure as well as that of the fundamental  $L1_0$ -(002)

peak drop substantially. In addition, the fraction of the A1-disordered phase increases, as indicated by the shift of the overlapping (002) peaks toward lower angles [Figs. 1(f)–1(h)]. Adding 14 at. % of Tb leads to the formation of a  $Pt_2Tb$  phase, as observed by the appearance of an additional (111) peak at  $2\theta = 20.4^\circ$  and confirmed by additional studies of Pt-Tb alloys (not shown). With further increase of the Tb amount, the PtTb phase forms, as can be seen by the presence of (200) and (020) peaks at  $2\theta = 20.41^\circ$  and  $30.18^\circ$ , respectively. By contrast to series I, the  $c$ -lattice parameter, extracted from the  $L1_0$ -(001) peak position, does not change with Tb content (Fig. 2). Thus, it can be concluded that Tb is not incorporated into the  $L1_0$  lattice, but rather forms a crystalline  $Pt_2Tb$  or PtTb phase [Fig. 1(i)]. As more and more of Pt is consumed in the PtTb intermetallic compound, mostly an Fe-rich A1-FePt phase remains with a very small fraction of  $L1_0$ -ordered FePt [Fig. 1(j)].

These structural properties were also investigated by TEM. A cross-section image of a  $(FePt)_{85}Tb_{15}$  film prepared at 530 °C is shown in Fig. 3(c). Close to the MgO(001) substrate surface, small crystalline areas are observed, while most of the remaining part of the thin film is amorphous. By contrast, mostly crystalline grains with different orientations corresponding to the disordered A1 FePt phase can be observed for the  $(FePt)_{81.5}Tb_{18.5}$  film deposited at 770 °C [Fig. 3(f)]. In this regard, Hellman *et al.* [35] have investigated in detail the amorphous-crystalline phase diagram of Tb-Fe thin films as function of deposition temperature and composition. They reported that at a deposition temperature of 530 °C an amorphous phase forms for Tb concentrations greater than 15 at. %, while for a deposition temperature of 770 °C an amorphous phase is only formed beyond 30 at. % of Tb. These observations are in agreement with our findings for series I, where  $(FePt)_{100-x}Tb_x$  samples with higher Tb content are becoming amorphous, while for series II only crystalline phases are observed. Moreover, the sample morphology of FePt and FePtTb films (with high Tb content) was investigated by AFM for both series. As shown in Figs. 3(a)–3(b) and

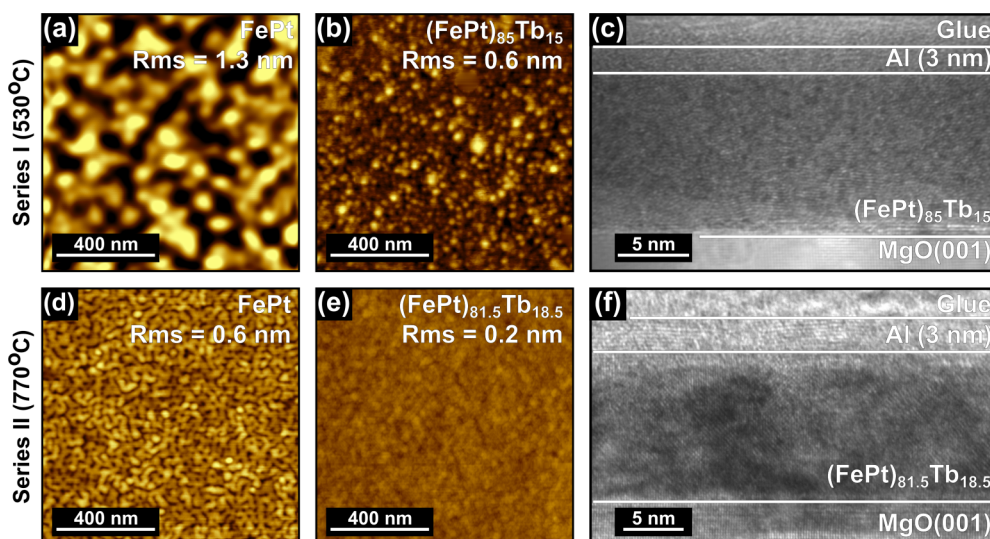


FIG. 3. AFM images of selected samples (a), (b) of series I and (d), (e) of series II; TEM cross-section images for the samples (c)  $(FePt)_{85}Tb_{15}$  deposited at 530 °C and (f)  $(FePt)_{81.5}Tb_{18.5}$  deposited at 770 °C.

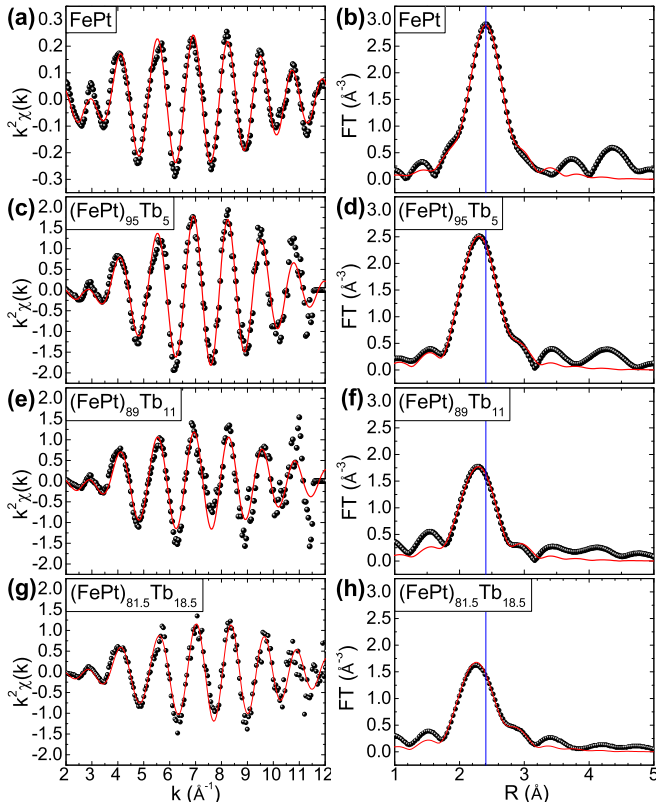


FIG. 4. EXAFS signals (left) at the Pt  $L_3$  edge and the corresponding amplitude of the Fourier transform (right) of the reference FePt and  $(\text{FePt})_{1-x}\text{Tb}_x$  samples with  $x = 5, 11,$  and  $18.5$  at. % of series II. Experimental data (scatter) and fits (line) are shown.

Figs. 3(d)–3(e) for both series, a strong island growth is revealed and with addition of Tb a substantial lowering of the root-mean-square roughness is observed.

#### IV. EXAFS CHARACTERIZATION

EXAFS studies have been carried out on selected samples of series II. A model based on Pt-Pt and Pt-Fe single-scattering paths generated by the  $L1_0$  tetragonal structure was used to study the FePt reference sample of series II: The fit has been performed on the Fourier-transformed space in the range  $1.5\text{--}3.5$  Å, where only the nearest-neighbor contributions are included for the  $k^2$ -weighted EXAFS data in the range  $4\text{--}12$  Å $^{-1}$  using Hanning windows with an apodization parameter  $dk$  of  $1$  Å $^{-1}$ . The free-fitting parameters used in

the analysis are the  $R_{\text{Pt-Pt}}$  and  $R_{\text{Pt-Fe}}$  distances, the shift of the energy origin  $\Delta E_0$ , the Debye-Waller factor ( $\sigma^2$ ), and the number  $N_{\text{Pt}}$  of Pt first neighbors, which is expected to be four in the fully  $L1_0$  ordered phase and six for the disordered A1 phase. In Figs. 4(a) and 4(b) the EXAFS signal of the FePt reference sample taken at the Pt  $L_3$  edge and the corresponding amplitude of the Fourier transform (FT) are presented. The resulting fitting parameters, summarized in Table II, indicate a high crystallographic quality with a significant difference between Pt-Pt and Pt-Fe distances, confirming the tetragonal structure of the  $L1_0$  phase. In order to highlight the effect of Tb addition on the chemical and structural properties of the ternary alloy, EXAFS spectra were collected on samples with different Tb content. A substitutional model was considered, aimed to verify if Tb atom substitutes the Fe or Pt atoms in the  $L1_0$  FePt lattice. According to the method applied for the  $L1_0$  FeCuPt system in Ref. [36], scattering paths were calculated after creating substitutional defects of Tb on both Pt ( $\text{Tb}_{\text{Pt}}$ ) and Fe ( $\text{Tb}_{\text{Fe}}$ ) sites in the  $L1_0$  FePt structure and all the data were fitted by a model based on a linear combination of Pt-Fe, Pt-Pt, Pt- $\text{Tb}_{\text{Pt}}$ , and Pt- $\text{Tb}_{\text{Fe}}$  paths on the Pt sites. For all samples, the fit excluded the presence of a Tb scattering element in the first neighbors shell around Pt. As a consequence, a pure FePt model has been considered to fit the FT data in the range  $R = 1.5\text{--}3.2$  Å and  $k = 2\text{--}10$  Å $^{-1}$ , with a fixed number of first-shell neighbors (equal to 12 for both the fcc and face-centered tetragonal structures). The results of selected samples are shown in Figs. 4(c)–4(h) and the resulting free-fitting parameters are summarized in Table II.

The effect of Tb on the FePt lattice can be evidenced by the contraction of all the distances and, more precisely, by the deformation of the tetragonal structure towards cubic symmetry, characteristic for the chemically disordered A1 FePt structure. Also, the increase of  $N_{\text{Pt}}$  value confirms this evolution. In fact,  $N_{\text{Pt}} = 6$  is expected for the A1-disordered crystallographic phase, where the positions of 12 nearest-neighbor atoms are equally distributed between the two elements of Fe and Pt; however, the experimental error does not allow for a precise determination of the degree of  $L1_0$  ordering.

#### V. MAGNETIC PROPERTIES

Room-temperature  $M$ - $H$  hysteresis loops of  $(\text{FePt})_{1-x}\text{Tb}_x$  ( $x = 0, 5, 11, 14,$  and  $18$  at. %) thin films of sample series I prepared at  $530$  °C are shown in Figs. 5(a)–5(e). All samples, including the FePt reference sample, reveal an in-plane easy axis of magnetization with a low coercivity at  $300$  K [Fig. 6(b)]. The effective magnetic anisotropy  $K_{\text{eff}}$

TABLE II. Fitting parameters of the Fourier transforms of the EXAFS signals for  $(\text{FePt})_{1-x}\text{Tb}_x$  samples with  $x = 0, 5, 11,$  and  $18.5$  at. % deposited at  $T = 700\text{--}770$  °C (series II).

Sample name	$N_{\text{Pt}}$ (atoms)	$R_{\text{Pt-Pt}}$ (Å)	$R_{\text{Pt-Fe}}$ (Å)	$\sigma^2$ (Å $^2$ )
FePt	$4 \pm 2$	$2.735 \pm 0.005$	$2.676 \pm 0.004$	$0.0010 \pm 0.0005$
$(\text{FePt})_{95}\text{Tb}_5$	$5 \pm 1$	$2.75 \pm 0.02$	$2.66 \pm 0.01$	$0.0050 \pm 0.0010$
$(\text{FePt})_{89}\text{Tb}_{11}$	$5 \pm 2$	$2.71 \pm 0.04$	$2.66 \pm 0.02$	$0.0070 \pm 0.0010$
$(\text{FePt})_{81.5}\text{Tb}_{18.5}$	$7 \pm 1$	$2.69 \pm 0.03$	$2.62 \pm 0.01$	$0.0040 \pm 0.0010$

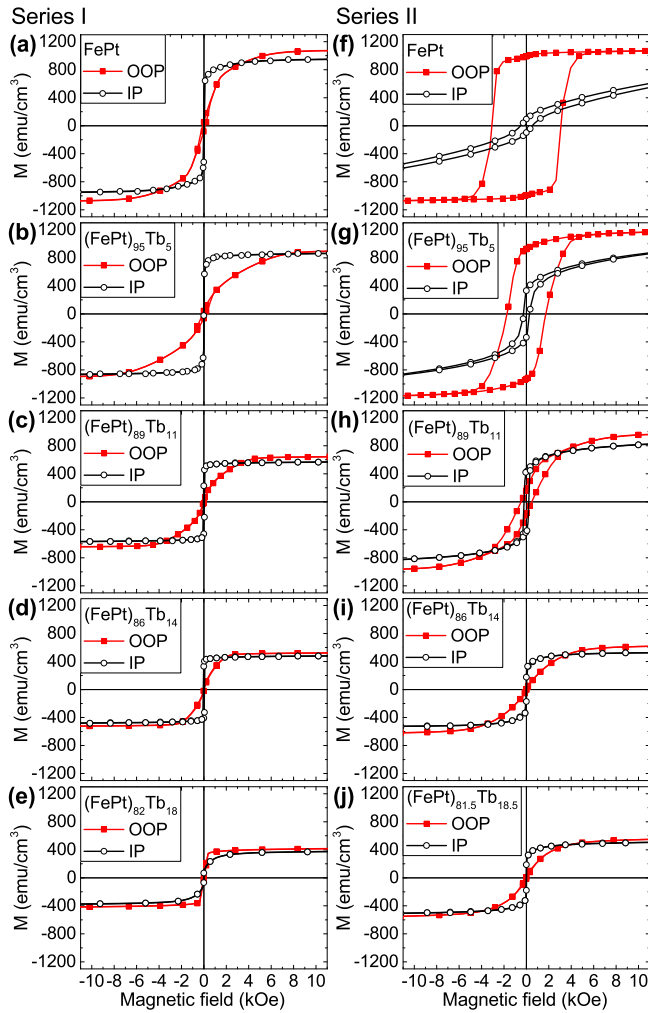


FIG. 5. OOP and IP  $M$ - $H$  hysteresis loops measured at 300 K for  $(\text{FePt})_{100-x}\text{Tb}_x$  films of (a)–(e) series I and (f)–(j) series II.

was extracted from the area difference between the averaged  $M$ - $H$  loops measured in out-of-plane (OOP) and in-plane (IP) geometry. Negative  $K_{\text{eff}}$  values confirm that the magnetic anisotropy is basically given by the magnetic shape anisotropy [Fig. 6(c)]. This behavior is in fact expected as most of the film consists of the chemically disordered A1 FePt phase and also becomes amorphous for samples with a Tb content higher than 11 at. % [see Figs. 1(c)–1(e)]. Most apparent is the impact of Tb on the saturation magnetization, which gets strongly reduced by more than 60% down to 400  $\text{emu}/\text{cm}^3$  at 18 at. % of Tb, as summarized in Fig. 6(a). This behavior can be explained by the antiferromagnetic coupling between the Fe and Tb moments, resulting in partial moment compensation, as will be discussed later.

By contrast, for series II prepared at 700–770 °C a pronounced  $L1_0$  (001) structure is obtained for the FePt reference film, resulting in strong PMA of about 1.3  $\text{MJ}/\text{m}^3$  [Fig. 5(f) and Fig. 6(c)]. However, with the addition of up to 5 at. % of Tb,  $K_{\text{eff}}$  and  $H_c$  are strongly reduced, as a result of reduced chemical order of the  $L1_0$  phase [Figs. 6(b) and 6(c)]. Further Tb addition leads to a full loss in PMA, resulting in an in-plane easy axis of magnetization with a small coercivity

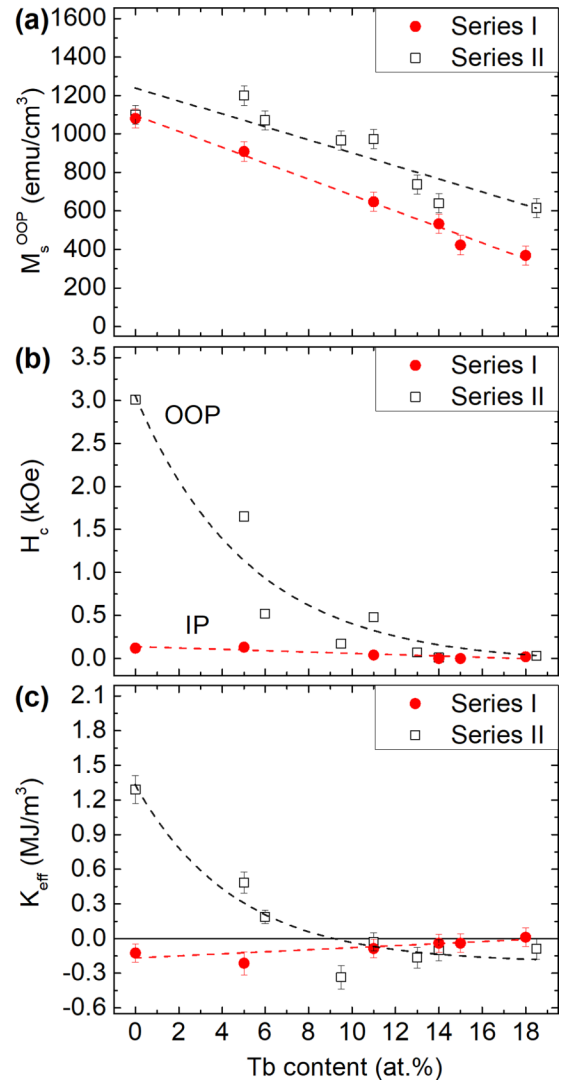


FIG. 6. Dependence of the (a) saturation magnetization, (b) coercivity (easy axis), and (c) effective magnetic anisotropy, obtained at 300 K, on the Tb content for both sample series. Lines are guide to the eyes.

at room temperature. In addition, a reduction in saturation magnetization is observed as well with increasing Tb content [Fig. 6(a)].

Since magnetic anisotropy and thus the orientational distribution of the Tb moments may vary with temperature, also the net magnetization is expected to change. To investigate this behavior,  $M$  versus  $T$  curves were measured, as shown in Fig. 7. Taking into account the magnetization easy-axis direction, the measurements were separated into two groups with (i) samples exhibiting out-of-plane and (ii) in-plane magnetic anisotropy. The samples were first saturated in a magnetic field of 70 kOe along the relevant easy-axis direction at room temperature and then cooled in zero field down to 25 K. Then, a guiding field of 1000 Oe was applied and the magnetization was measured along the easy-axis direction during heating up to 325 K. FePt-Tb samples with up to 11 at. % Tb of series II showed a slight increase in magnetization with decreasing temperature due to reduced thermal agitation of the dominant

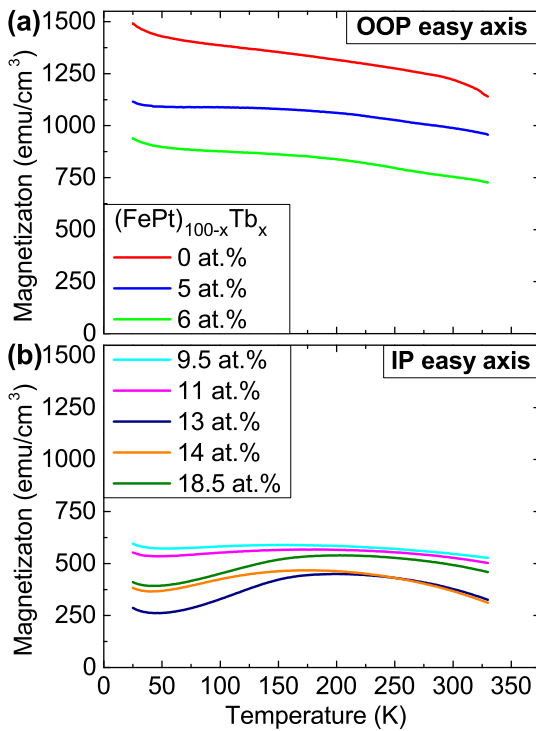


FIG. 7. Magnetization in the easy-axis direction (a) OOP and (b) IP depending on the Tb content for  $(\text{FePt})_{100-x}\text{Tb}_x$  film samples of series II.

total Fe moment following basically the behavior of the FePt reference sample. By contrast, FePt-Tb samples with larger Tb content showed a reduction of the magnetization at a certain temperature. This behavior is typically observed in Tb-rich Tb-Fe alloys [22,37], where the magnetic moment of Tb, which is preferably antiparallel aligned to Fe, increases more strongly than the Fe moment, resulting in a net reduction in the total magnetic moment.

We have also investigated the temperature-dependent magnetic properties of sample series I. Exemplarily,  $M$ - $H$  hysteresis loops taken at different temperatures for the  $(\text{FePt})_{86}\text{Tb}_{14}$  film sample are shown in Figs. 8(a)–8(c). Here, most interestingly, a spin-reorientation transition (SRT) indicated by the appearance of strong PMA with an out-of-plane easy-axis magnetization is observed at temperatures below 250 K. The transition temperature for this sample series was determined by plotting  $K_{\text{eff}}$  as function of temperature, as summarized in Fig. 8(d). In this case, positive  $K_{\text{eff}}$  values correspond to PMA, while negative values indicate in-plane magnetic anisotropy. As shown in Fig. 8(e), the SRT temperature increases from 120 K to above room temperature by increasing the Tb content from 11 to 18 at. %, respectively.

Typically, in amorphous Tb-Fe-based alloy thin films the origin of PMA is associated with an anisotropic chemical short-range order (SRO), where atomic next-neighbor distances and number of Tb-Tb, Fe-Fe, and Tb-Fe pairs are different in out-of-plane and in-plane direction (pair-order anisotropy). In the out-of-plane direction (growth direction), a preference exists for Tb-Fe near-neighbor pairing [38–46], which can be induced by selective resputtering effects during

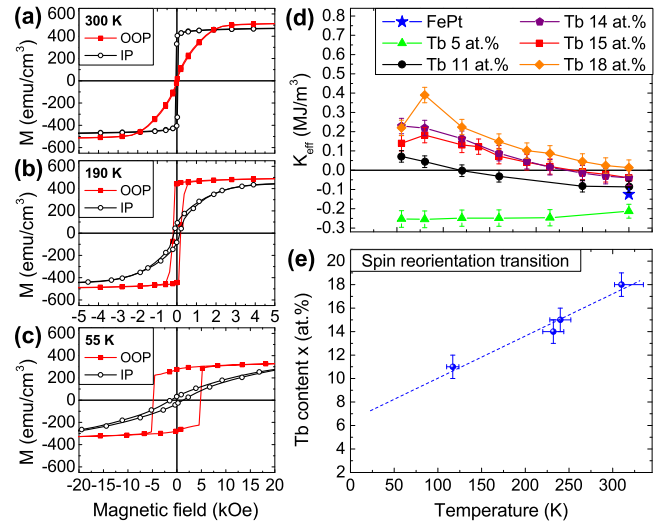


FIG. 8. Out-of-plane and in-plane  $M$ - $H$  hysteresis loops of the  $(\text{FePt})_{86}\text{Tb}_{14}$  film of series I measured at (a) 300 K, (b) 190 K, and (c) 55 K. Please note that magnetic-field scale in (a) and (b) is different from (c). (d) Effective magnetic anisotropy and (e) spin-reorientation transition temperature of  $(\text{FePt})_{100-x}\text{Tb}_x$  film samples of series I.

sputter deposition at room temperature [38,47]. For our FePt-Tb thin films of series I, we observe a slight increase in  $K_{\text{eff}}$  towards positive values at room temperature with higher Tb content [Fig. 6(c)], which is accompanied by a higher degree of amorphization. Thus, the presence of an anisotropic chemical SRO with a preference of Tb-Fe near-neighbor pairing is expected to be the origin of PMA similar to amorphous Tb-Fe-based alloys [22,37]. As the saturation magnetization gets reduced with lowering the temperature [see Figs. 8(a)–8(c), Fig. 9], the contribution of the magnetic shape anisotropy gets weaker and eventually gets overcompensated by the PMA (due to pair-order anisotropy), resulting in a SRT.

In order to see the variation of the magnetization in particular below the SRT, we plotted the out-of-plane remanent magnetization  $M_r^{\text{OOP}}$  as a function of temperature (Fig. 9). Above the SRT temperature, the  $M_r^{\text{OOP}}$  values are rather low as the systems exhibit an in-plane easy-axis orientation. By

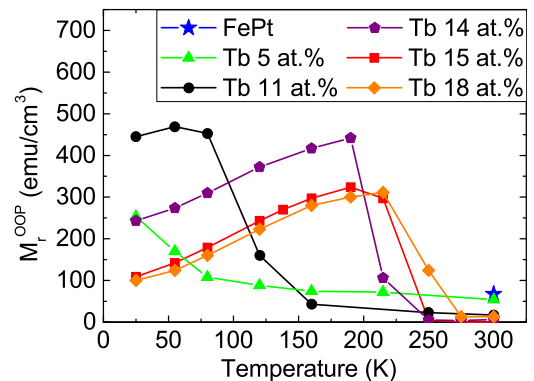


FIG. 9. Out-of-plane remanence magnetization as function of temperature of  $(\text{FePt})_{100-x}\text{Tb}_x$  film samples of series I.

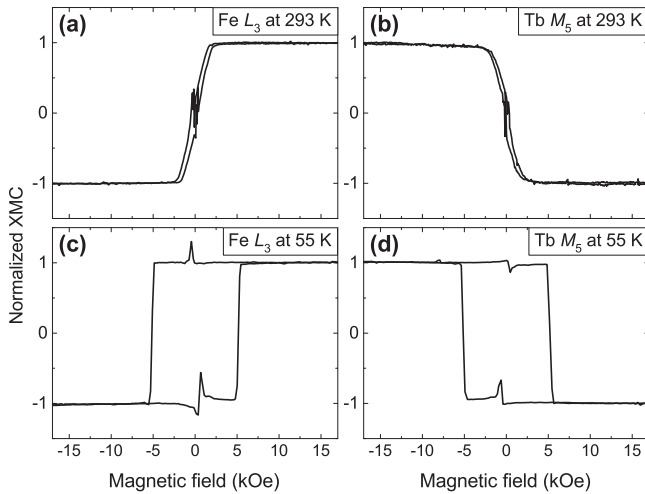


FIG. 10. XMCD element-specific hysteresis loops of Fe and Tb measured at (a), (b) 293 K and (c), (d) 55 K. The dips in the hysteresis loops close to zero magnetic field are x-ray intensity artifacts which are typical for TEY detection [53].

crossing the SRT temperature, a pronounced increase in  $M_r^{\text{OOP}}$  is observed, which is consistent with the onset of PMA, shown by the sign change of  $K_{\text{eff}}$  [Fig. 8(d)]. Further lowering of the temperature results in a decreasing  $M_r^{\text{OOP}}$ , which is associated with an increasing Tb net moment, approaching the expected compensation at higher Tb contents.

In order to discern the influence of each element on the net magnetization and reveal the relative orientation of Fe and Tb magnetic moments, XMCD measurements have been performed in total electron yield mode at the Fe  $L_{2,3}$  and Tb  $M_{4,5}$  edges (at 293 and 55 K) for the  $(\text{FePt})_{86}\text{Tb}_{14}$  film sample of series I. All spectra have been measured in an applied magnetic field up to 20 and 40 kOe at 293 and 55 K, respectively. In order to acquire the XMCD data, the field has been reversed. The shape of the Fe spectrum (not shown) corresponds to the typical metallic Fe configuration [48] and there are no signs of oxidation [49]. As expected, an opposite sign of the dichroism signal observed at the Fe and Tb edges, indicating an antiferromagnetic alignment of the two magnetic moments [22], was observed.

Element-specific magnetic hysteresis loops have been recorded by measuring the peak height of the Tb  $M_5$  and Fe  $L_3$  absorption edges as a function of the applied magnetic field for the  $(\text{FePt})_{86}\text{Tb}_{14}$  film (series I) in out-of-plane geometry at 293 K [Figs. 10(a) and 10(b)] and 55 K [Figs. 10(c) and 10(d)]. The loops of Tb and Fe are inverted and show exactly the same shape of magnetic reversal behavior, implying strong antiferromagnetic exchange interaction between these two elements. Furthermore, a change in easy axis of magnetization from in-plane to out-of-plane orientation is observed at 55 K, which is in nice agreement with SQUID-VSM results [Figs. 8(a)–8(c)]. The same correspondence of the element-specific hysteresis loops shape was observed for the samples of series II, indicating antiferromagnetic exchange interaction between Tb and Fe as well (not shown). It is worth noting that this behavior is quite different compared to FePt with Nb addition where XMCD studies revealed no magnetic

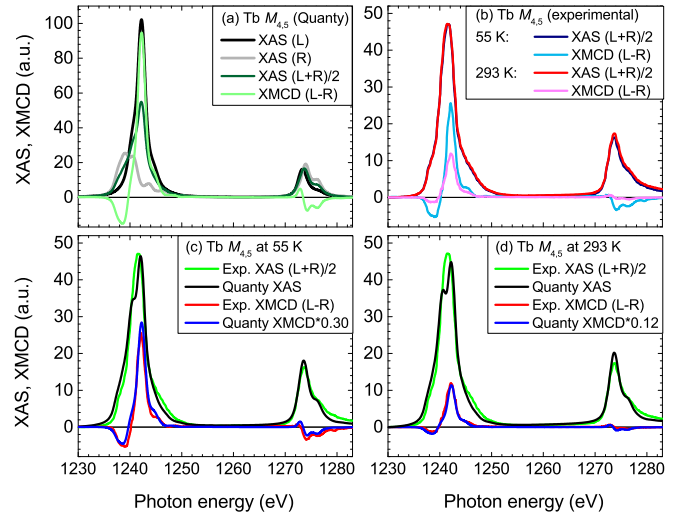


FIG. 11. (a) Calculated  $L$  and  $R$ -polarized Tb  $M_{4,5}$  XAS spectra using QUANTY multiplet theory are shown together with the corresponding nonmagnetic average ( $L/2 + R/2$ ) and difference ( $L - R$ ) XMCD spectrum. In (b) the experimental nonmagnetic average and the XMCD spectra of  $(\text{FePt})_{86}\text{Tb}_{14}$  (series I) for 55 and 293 K are shown. Calculated XAS spectra of  $(\text{FePt})_{86}\text{Tb}_{14}$  sample (series I) are shown for (c) 55 K and (d) 293 K together with corresponding experimental XMCD spectra.

correlation between Fe and Nd above 6 at. %, most likely due to structural phase separations occurring in these films [21].

In order to extract the spin ( $m_s$ ) and orbital moment ( $m_l$ ) of Fe, sum rules were applied, giving a total magnetic moment of Fe per atom of  $1.92\mu_B$  ( $m_s = 2.00 \pm 0.30\mu_B$ ,  $m_l = -0.08 \pm 0.30\mu_B$ ) at room temperature and  $2.13\mu_B$  ( $m_s = 2.13 \pm 0.11\mu_B$ ,  $m_l = 0.00 \pm 0.05\mu_B$ ) at 55 K.

Unfortunately sum rules cannot easily be applied for the Tb  $M_{4,5}$  edges, due to the magnetic dipole operator ( $T_Z$ ) and  $M_{4,5}$  mixing phenomena [50,51]. Therefore, we performed atomic multiplet calculations (Fig. 11) using the QUANTY code from Haverkort *et al.* [52]. This calculation provides XAS spectra for any given light polarization, here left ( $L$ ), right ( $R$ ), and linear ( $Z$ ) polarized. In Fig. 11(a) the calculated  $L$  and  $R$ -polarized XAS spectra are presented together with the nonmagnetic average ( $L/2 + R/2$ ) and the corresponding ( $L-R$ ) XMCD spectrum. Figure 11(b) shows the experimental nonmagnetic average and the XMCD spectra at 55 and 293 K of  $(\text{FePt})_{86}\text{Tb}_{14}$  (series I). Further, in Figs. 11(c) and 11(d) these experimental data are presented together with the corresponding QUANTY fits for both temperatures. The nonmagnetic spectra have been fitted by a superposition of simulated  $L$ ,  $R$ , and  $Z$ -polarized spectra. In addition, the simulated ( $L-R$ ) XMCD spectra have been scaled down to match the measured XMCD spectrum by a factor of 0.30 for 55 K and 0.12 for 293 K. XMCD and XAS spectra are in almost perfect agreement with respect to the QUANTY simulation results. Especially, the XMCD spectra resemble every tiny feature present in the simulations. Therefore, we can firmly conclude that the Tb is in an almost pure  $\text{Tb}^{3+}$  state and the spin and orbital momenta are exactly the same as given from theory, but not saturated and therefore simply reduced by a single factor for each temperature. The full

saturated expectation values from QUANTY for  $\text{Tb}^{3+}$  are for the orbital momentum  $L = 3.057$  and spin momentum  $S = 2.943$ , which are also in perfect agreement with the results published earlier by Teramura *et al.* [50]. From the fit and the reduction factors (0.30 for 55 K and 0.12 for 293 K), we obtain for our sample a total magnetic moment  $m_{\text{tot}}$  (55 K) =  $(L + 2 \times S) \mu_B = (0.92 + 2 \times 0.88) \mu_B = 2.68 \mu_B$  and  $m_{\text{tot}}$  (293 K) =  $(0.37 + 2 \times 0.35) \mu_B = 1.07 \mu_B$ . Both values are clearly far below saturation. One of the main reasons for the large discrepancy in magnetic moment of Tb is based on the fact that we probe with XMCD only the projection of the magnetic moment onto the photon beam direction. For sperimagnetic TbFe alloys, it is well known that the magnetic moments are not collinearly aligned but reveal a large angle distribution depending on the local magnetic anisotropy and exchange couplings, as already mentioned, which will certainly result in a strongly reduced magnetic moment in out-of-plane direction.

## VI. SUMMARY

FePt thin films deposited on MgO(001) at 530 °C show rather weak  $L1_0$  chemical ordering. With addition of Tb, a shift of the  $c$ -axis lattice parameter is observed, indicating that Tb is likely located at interstitial sites adding elastic stress to the lattice, which eventually results in full amorphization of the films. Interestingly, a spin-reorientation transition from in-plane easy axis towards out-of-plane easy axis of magnetization was observed at low temperatures. The onset tem-

perature of SRT can be increased towards room temperature with increasing Tb content. Higher deposition temperature of 700–770 °C promotes chemical ordering and (001) orientation growth of the  $L1_0$  FePt phase with strong PMA. With addition of Tb, a reduction in  $L1_0$  ordering and PMA is observed. At a Tb content higher than 11 at. % the formation of crystalline Tb-Pt phases is observed. X-ray magnetic circular dichroism studies show that for both sample series, Tb and Fe are strongly antiferromagnetic exchange coupled but with a non-collinear alignment of the magnetic moments, thus forming a sperimagnetic system with reduced saturation magnetization.

## ACKNOWLEDGMENTS

We would like to thank O. Lik for the assistance in sample preparation, W. Reiber for performing RBS measurements, M. Lindorf and B. Knoblich for TEM sample preparation and imaging, and O. Ciubutariu, M. Heigl, and R. Wendler for assistance at the HZB beamline. The authors are thankful for the allocation of synchrotron radiation beam time and acknowledge the financial support from HZB (Project No. 16103747-ST). This work was financially supported by the German Research Foundation (DFG Grant No. AL618/31-1). Financial support for developing and building the PM2-VEKMAG beamline and VEKMAG end-station was provided by HZB and BMBF (Grants No. 05K10PC2, No. 05K10WR1, and No. 05K10KE1), respectively. S. Rudorff is acknowledged for technical support.

- 
- [1] R. F. C. Farrow, D. Weller, R. F. Marks, and M. F. Toney, *J. Appl. Phys.* **79**, 5967 (1996).
  - [2] A. Hotta, T. Ono, M. Hatayama, K. Tsumura, N. Kikuchi, S. Okamoto, O. Kitakami, and T. Shimatsu, *J. Appl. Phys.* **115**, 17B712 (2014).
  - [3] J. Lyubina, B. Rellinghaus, O. Gutfleisch, and M. Albrecht, in *Handbook of Magnetic Materials*, edited by K. H. J. Buschow (Elsevier, Amsterdam, 2011), Vol. 19, pp. 291–395.
  - [4] D. Weller, O. Mosendz, G. Parker, S. Pisana, and T. S. Santos, *Phys. Status Solidi A* **210**, 1245 (2013).
  - [5] D. Weller, G. Parker, O. Mosendz, A. Lyberatos, D. Mitin, N. Y. Safonova, and M. Albrecht, *J. Vac. Sci. Technol. B* **34**, 060801 (2016).
  - [6] D. Suess and T. Schrefl, *Appl. Phys. Lett.* **102**, 162405 (2013).
  - [7] K. Hono, Y. Takahashi, G. Ju, J. Thiele, A. Ajan, X. Yang, R. Ruiz, and L. Wan, *MRS Bull.* **43**, 93 (2018).
  - [8] M. T. Kief and R. H. Victora, *MRS Bull.* **43**, 87 (2018).
  - [9] T. Ono, H. Nakata, T. Moriya, N. Kikuchi, S. Okamoto, O. Kitakami, and T. Shimatsu, *AIP Adv.* **6**, 056011 (2016).
  - [10] M. Albrecht and C. Brombacher, *Phys. Status Solidi A* **210**, 1272 (2013).
  - [11] C. Brombacher, H. Schletter, M. Daniel, P. Matthes, N. Jöhrmann, M. Maret, D. Makarov, M. Hietschold, and M. Albrecht, *J. Appl. Phys.* **112**, 073912 (2012).
  - [12] M. Maret, C. Brombacher, P. Matthes, D. Makarov, N. Boudet, and M. Albrecht, *Phys. Rev. B* **86**, 024204 (2012).
  - [13] D. B. Xu, J. S. Chen, T. J. Zhou, and G. M. Chow, *J. Appl. Phys.* **109**, 07B747 (2011).
  - [14] J. Park, Y.-K. Hong, S.-G. Kim, L. Gao, and J.-U. Thiele, *J. Appl. Phys.* **117**, 053911 (2015).
  - [15] K. Kang, Z. G. Zhang, C. Papusoi, and T. Suzuki, *Appl. Phys. Lett.* **82**, 3284 (2003).
  - [16] M. L. Yan, Y. F. Xu, X. Z. Li, and D. J. Sellmyer, *J. Appl. Phys.* **97**, 10H309 (2005).
  - [17] B. S. D. Ch. S. Varaprasad, Y. K. Takahashi, J. Wang, T. Ina, T. Nakamura, W. Ueno, K. Nitta, T. Uruga, and K. Hono, *Appl. Phys. Lett.* **104**, 222403 (2014).
  - [18] Y. Z. Zhou, J. S. Chen, G. M. Chow, and J. P. Wang, *J. Appl. Phys.* **95**, 7495 (2004).
  - [19] C. Feng, Q. Zhan, B. Li, J. Teng, M. Li, Y. Jiang, and G. Yu, *Appl. Phys. Lett.* **93**, 152513 (2008).
  - [20] F. Radu and J. Sánchez-Barriga, in *Novel Magnetic Nanostructures*, Micro and Nano Technologies, edited by N. Domracheva (Elsevier, Amsterdam, 2018), p. 267.
  - [21] D. B. Xu, C. J. Sun, J. S. Chen, S. M. Heald, B. Sanyal, R. A. Rosenberg, T. J. Zhou, and G. M. Chow, *J. Phys. D* **48**, 255001 (2015).
  - [22] B. Hebler, S. Böttger, D. Nissen, R. Abrudan, F. Radu, and M. Albrecht, *Phys. Rev. B* **93**, 184423 (2016).
  - [23] W. Bailey, P. Kabos, F. Mancoff, and S. Russek, *IEEE Trans. Magn.* **37**, 1749 (2001).
  - [24] C. D. Stanciu, F. Hansteen, A. V. Kimel, A. Kirilyuk, A. Tsukamoto, A. Itoh, and Th. Rasing, *Phys. Rev. Lett.* **99**, 047601 (2007).

- [25] A. Kirilyuk, A. V. Kimel, and Th. Rasing, *Rev. Mod. Phys.* **82**, 2731 (2010).
- [26] A. Hassdenteufel, B. Hebler, C. Schubert, A. Liebig, M. Teich, M. Helm, M. Aeschlimann, M. Albrecht, and R. Bratschitsch, *Adv. Mater.* **25**, 3122 (2013).
- [27] A. Hassdenteufel, C. Schubert, B. Hebler, H. Schultheiss, J. Fassbender, M. Albrecht, and R. Bratschitsch, *Opt. Express* **22**, 10017 (2014).
- [28] A. Hassdenteufel, C. Schubert, P. Reinhardt, P. Richter, J. Schmidt, M. Fronk, G. Salvan, D. R. T. Zahn, M. Helm, R. Bratschitsch, and M. Albrecht, *Appl. Phys. Lett.* **105**, 112403 (2014).
- [29] B. Hebler, A. Hassdenteufel, P. Reinhardt, H. Karl, and M. Albrecht, *Front. Mater.* **3**, 8 (2016).
- [30] A. Hassdenteufel, J. Schmidt, C. Schubert, B. Hebler, M. Helm, M. Albrecht, and R. Bratschitsch, *Phys. Rev. B* **91**, 104431 (2015).
- [31] M. S. El Hadri, P. Pirro, C.-H. Lambert, S. Petit-Watelot, Y. Quessab, M. Hehn, F. Montaigne, G. Malinowski, and S. Mangin, *Phys. Rev. B* **94**, 064412 (2016).
- [32] T. Noll and F. Radu, in *Proceedings 9th Edition of the Mechanical Engineering Design of Synchrotron Radiation Equipment and Instrumentation Conference (MEDSI'16), Barcelona, Spain* (JACoW, Geneva, Switzerland, 2017), pp. 370–373.
- [33] B. Ravel and M. Newville, *J. Synchrotron Radiat.* **12**, 537 (2005).
- [34] A. L. Ankudinov, B. Ravel, J. J. Rehr, and S. D. Conradson, *Phys. Rev. B* **58**, 7565 (1998).
- [35] F. Hellman, R. B. van Dover, S. Nakahara, and E. M. Gyorgy, *Phys. Rev. B* **39**, 10591 (1989).
- [36] S. Laureti, C. Brombacher, D. Makarov, M. Albrecht, D. Peddis, G. Varvaro, and F. D'Acapito, *J. Appl. Crystallogr.* **47**, 1722 (2014).
- [37] C. Schubert, B. Hebler, H. Schletter, A. Liebig, M. Daniel, R. Abrudan, F. Radu, and M. Albrecht, *Phys. Rev. B* **87**, 054415 (2013).
- [38] R. J. Gambino and J. J. Cuomo, *J. Vac. Sci. Technol.* **15**, 296 (1978).
- [39] R. B. van Dover, M. Hong, E. M. Gyorgy, J. F. Dillon, Jr., and S. D. Albiston, *J. Appl. Phys.* **57**, 3897 (1985).
- [40] C. J. Robinson, M. G. Samant, and E. E. Marinero, *Appl. Phys. A* **49**, 619 (1989).
- [41] M. Tewes, J. Zweck, and H. Hoffmann, *J. Magn. Magn. Mater.* **95**, 43 (1991).
- [42] V. G. Harris, K. D. Aylesworth, B. N. Das, W. T. Elam, and N. C. Koon, *Phys. Rev. Lett.* **69**, 1939 (1992).
- [43] V. G. Harris, W. T. Elam, N. C. Koon, and F. Hellman, *Phys. Rev. B* **49**, 3637(R) (1994).
- [44] F. Hellman and E. M. Gyorgy, *Phys. Rev. Lett.* **68**, 1391 (1992).
- [45] A. Hernando, C. Prados, and C. Prieto, *J. Magn. Magn. Mater.* **157–158**, 501 (1996).
- [46] T. C. Hufnagel, S. Brennan, P. Zschack, and B. M. Clemens, *Phys. Rev. B* **53**, 12024 (1996).
- [47] V. G. Harris and T. Pokhil, *Bull. Mater. Sci.* **22**, 503 (1999).
- [48] C. T. Chen, Y. U. Idzerda, H. J. Lin, N. V. Smith, G. Meigs, E. Chaban, G. H. Ho, E. Pellegrin, and F. Sette, *Phys. Rev. Lett.* **75**, 152 (1995).
- [49] B. Gilbert, J. E. Katz, J. D. Denlinger, Y. Yin, R. Falcone, and G. A. Waychunas, *J. Phys. Chem. C* **114**, 21994 (2010).
- [50] Y. Teramura, A. Tanaka, B. T. Thole, and T. Jo, *J. Phys. Soc. Jpn.* **65**, 3056 (1996).
- [51] T. Jo, *J. Electron Spectrosc. Relat. Phenom.* **86**, 73 (1997).
- [52] M. W. Haverkort, G. Sangiovanni, P. Hansmann, A. Toschi, Y. Lu, and S. Macke, *Eur. Phys. Lett.* **108**, 57004 (2014).
- [53] E. Goering, A. Fuss, W. Weber, J. Will, and G. Schütz, *J. Appl. Phys.* **88**, 5920 (2000).